Locating the largest event observed on Mars with multi-orbit surface waves

M. Panning, W. Banerdt, C. Beghein, S. Carrasco, S. Ceylan, J. Clinton, P. Davis, M. Drilleau, D. Giardini, A. Khan, et al.

Locating the largest event observed on Mars with multi-orbit surface waves

M. P. Panning[1], W. B. Banerdt[1], C. Beghein[2], S. Carrasco[3], S. Ceylan[4], J. F. Clinton[4], P. Davis[2], M. Drilleau[5], D. Giardini[4], A. Khan[4], D. Kim[4], B. Knapmeyer-Endrun[3], J. Li[2], P. Lognonné[6], S. C. Stähler[4], G. Zenhäusern[4]

[1]Jet Propulsion Laboratory, California Institute of Technology, USA
[2]University of California, Los Angeles, USA
[3]University of Cologne, Germany
[4]ETH Zürich, Switzerland
[5]ISAE Supaero, Toulouse, France
[6]Université Paris Cité, Institut de physique du globe de Paris, CNRS, Paris, France

Key Points:

- The M_W 4.7 S1222a event is the first marsquake large enough for multi-orbit surface wave location independent of a priori seismic velocity
- Using measurements of R1, R2, and R3 Rayleigh waves, we determine an epicentral distance consistent with that estimated from body waves
- Elliptical particle motion is observed for Rayleigh wave arrivals broadly consistent with the backazimuth identified from body waves

Corresponding author: Mark P. Panning, `Mark.P.Panning@jpl.nasa.gov`

Abstract

Prior to the 2018 landing of the InSight mission, the InSight science team proposed locating marsquakes using multiple orbit surface waves, independent of seismic velocity models, for events larger than $M_W 4.6$. The S1222a $M_W 4.7$ of May 4, 2022 is the largest marsquake recorded and the first large enough for this method. Group arrivals of the first three orbits of Rayleigh waves are determined to derive the group velocity, epicentral distance, and origin time. The mean distance of 36.9 ± 0.3 degrees agrees with the Marsquake Service (MQS) distance based on body wave measurements of 37.0 ± 1.6 degrees. The origin time from surface waves is systematically later than the MQS origin time by 20 seconds. Backazimuth estimation is similar to body wave estimations from MQS although suggesting a shift to the south. Backazimuth estimates from R2 and R3 are more scattered, but do show clear elliptical motion.

Plain Language Summary

Waves that move along the surface all the way around the planet of Mars can be used to figure out where a marsquake occurred without knowing in advance how fast the waves move through the planet, because we know how big the planet is. Before InSight got to Mars, we predicted that we would be able to see these waves if an event was big enough, and on May 4, 2022, we finally saw a marsquake large enough to test this approach. Based on the timing of the arrivals of these waves, we were able to figure out the distance and timing of the marsquake. The results agreed well with the approach we had been using for smaller events, giving us additional confidence in our tools for figuring out where marsquakes have happened.

1 Introduction

On May 4, 2022, the 1222nd sol of the InSight mission (Banerdt et al., 2020), the SEIS instrument (Lognonné et al., 2019) recorded the largest event of the mission to date, called S1222a (Kawamura et al., 2022). The moment magnitude of the event is estimated as $M_W 4.7$, meaning it is approximately 5 times larger in terms of seismic moment than the second largest observed event (S0976a, Horleston et al., 2022). The large moment release of this event has opened up a variety of new observations not possible with previous smaller events.

In particular, this event is the first that allows us to test a single station location method proposed before the launch of the mission that makes use of the observation of multiple orbit surface waves (Panning et al., 2015; Khan et al., 2016). Prior to the mission, there was ~~some~~ concern about how well the mission ~~would be able to~~could locate events with a single station when the seismic velocity structure of Mars was not well-known in advance. While *a priori* models of the interior velocity structure were available before landing (e.g. Khan et al., 2018; Bagheri et al., 2019; Smrekar et al., 2019) and body wave location methods that depend on the initially unknown velocity structure have been ~~very~~ successful in locating events (Durán et al., 2022), proposing a method that did not directly depend on any knowledge of the velocity structure (beyond assuming the structure is spherically symmetric) allowed for a plan to verify locations based on body waves.

Multiple orbit surface waves have paths around the sphere of a planet that allow for multiple arrivals in the minutes and hours after the origin time of the event. For Rayleigh waves, recorded on the vertical and horizontal component in the great-circle plane connecting the source and receiver, we refer to these as R1, R2, R3, etc. R1 represents surface wave energy that takes the shortest distance around the planet (or minor arc) to the station, while R2 propagates away from the source 180 degrees away from the direction of R1 and takes the longer path around the planet (or major arc). R3 follows the minor arc, but has an additional full circuit around the planet compared to R1. If we

assume a spherically symmetric model of velocity structure, because R3 and R1 differ only by the complete trip around the planet, we are able to determine the velocity of surface wave propagation and therefore also the epicentral distance and origin time without knowing the velocity in advance (Panning et al., 2015). A ~~simple~~ set of 3 equations determines the 3 unknowns as

$$U = \frac{2\pi}{t_{R3} - t_{R1}} \tag{1}$$

$$\Delta = \pi - \frac{1}{2}U(t_{R2} - t_{R1}) \tag{2}$$

$$t_0 = t_{R1} - \frac{\Delta}{U}, \tag{3}$$

where ~~R1, R2, and R3~~ t_{R1}, t_{R2}, and t_{R3} are the arrival times of the multi-orbit Rayleigh waves ~~(note that the travel times are written in italics, while the waves themselves are written without italics)~~, U is the great-circle average group velocity of the Rayleigh wave (in radians per second measured on the great circle), and Δ and t_0 are the epicentral distance and origin time of the event, respectively. In addition to epicentral distance and origin time, the full event location also requires an estimation of the backazimuth, and this can be obtained from the elliptical particle motion of the Rayleigh waves (see section 3).

In order for this method to be used, however, an event needs to be large enough so that R3 can be observed. On Earth, R3 can be reliably observed at quiet stations by $M_W 5.5$-6, but Panning et al. (2015) argued that with the smaller radius of Mars, R3 should be reliably observable around $M_W 4.6$ on Mars for a vertical instrument noise of 10^{-9} m/s^2/Hz$^{1/2}$ in the surface wave bandwidth. With the estimates of martian seismicity available at the time, 1-10 events of $M_W 5.3$ were predicted over the course of the mission, and so it was expected that this method could be applied to several of the largest events observed by InSight. In reality, both the daily wind-induced noise that is much larger than 10^{-9} m/s^2/Hz$^{1/2}$ (e.g. Lognonné et al., 2020) and a seismicity generating mostly $M_W < 4$ events (Giardini et al., 2020; Clinton et al., 2020; Brinkman et al., 2021; Jacob et al., 2022; Ceylan et al., 2022) has made this method impossible ~~until~~for events prior to S1222a. This was, therefore, the first event that exceeded the pre-mission estimated magnitude threshold, and it provides an excellent test case for the method at last.

2 Measuring multi-orbit Rayleigh wave arrival times

Panning et al. (2015) and Khan et al. (2016) proposed a straightforward approach to picking the ~~R1–R3~~t_{R1} to t_{R3} arrival times and demonstrated it using terrestrial and synthetic Martian data (called Method 1 in following figures), respectively. As illustrated in Figure 1, a series of narrow-band filters of the data (InSight Mars SEIS Data Service, 2019) are performed on center frequencies spaced in 15% intervals. For each center frequency, zero-phase (i.e. two pass) 2nd-order Butterworth bandpass filtering with ~~2 corners and a 30% width~~ a width of 30% of the central frequency was performed with Obspy software (Krischer et al., 2015), and then the envelope was calculated, and picks were made in frequency bands where a clear peak was observable. In the frequency band between 0.01 and 0.1 Hz, where we looked for surface wave energy, the raw data shows evidence of many glitches common to InSight data (e.g. Scholz et al., 2020; Kim et al., 2021; Ceylan et al., 2021). In particular, a large glitch arrives ~~very~~ close to the R3 arrival time, and so all measurements are made on deglitched data. Deglitching of the event data was carried out ~~in two steps. First, we applied~~with the UCLA method (with more recent modifications; see supplementary material) described in Scholz et al. (2020) on raw 20 samples per second velocity channels BHU, BHV, BHW with an additional step to identify glitches hidden in the event coda that show up as steps in displacement. ~~To test for false identifications and missing glitches, the second step involved integration of the deglitched velocity data to displacement. Unlike the majority of the noise, glitches are primarily either positive or negative velocity pulses. Upon integration remaining glitches, both spurious and missed ones, then~~
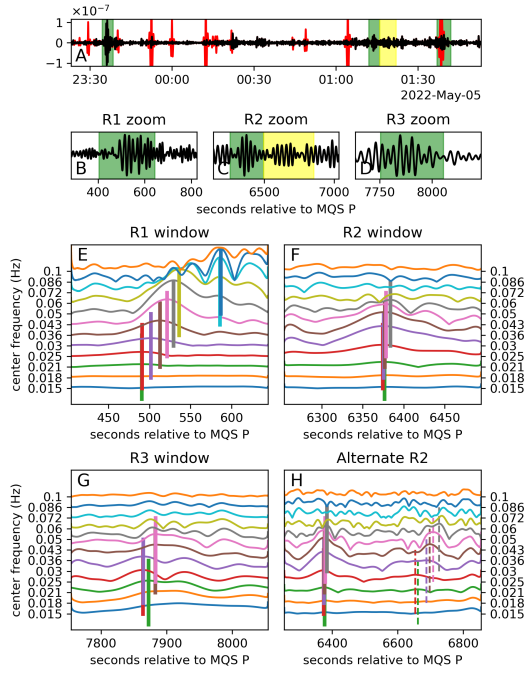
Figure 1. (A) 2.5 hours of raw (red) and deglitched (black) vertical component data starting with the MQS origin time of 23:23:06.57 UTC on May 4, 2022, bandpass filtered between 0.02 and 0.05 Hz. (B) Zoom into the R1 arrival window bandpass filtered between 0.02 and 0.09 Hz with the window for the ~~filter banks~~set of narrow-band filters shown in panel D highlighted in green. (C and D) Zoom window showing R2 and R3 arrival times, respectively, filtered between 0.02 and 0.04 Hz. The green boxes highlight the windows for filter banks in panels F and G, while the yellow box indicates the additional R2 window considered in panel H. (E-H) Filter banks where the central frequency of each trace is shown on the left where all traces are band-passed within a window extending 30% from the central frequency. Picks for Method 1 are shown with vertical bars where the color indicates which frequency band the pick was made on. Dashed lines in (H) show the alternate R2 arrival time picks discussed in the text.

114 ~~show up as sharp steps in the data. These were identified manually and removed by subtracting the~~
115 ~~corresponding glitch template. Several glitches were detected in the earthquake coda that were not~~
116 ~~detected in the higher frequency data, the coda amplitudes being so large (supplementary material)~~
117 ~~The glitch occurring at the time of R3 presented an initial difficulty in that the glitch template and~~
118 ~~the R3 signal are not orthogonal. Thus fitting the template and removing it runs the risk of removing~~
119 ~~some R3 signal. Ideally if a good synthetic were found a joint fit would be better. However with~~
120 ~~neither source nor path knowledge given the limitations of a one station recording this is not at this~~
121 ~~time practical.~~

122 Four different methods that differ ~~primarily~~ in the precise filter definition and pick-
123 ing method are used for picking ~~R1-R3~~t_{R1}-t_{R3} to be confident in the location determined,
124 with Method 1 described above. Method 2 is a similar approach performed routinely by
125 the Marsquake Service (MQS; Clinton et al., 2018) on half-octave wide frequency bands
126 and uses the arrival times included in their standard catalog (InSight Marsquake Ser-

vice, 2022). Common picks for each of ~~R1-R3~~t_{R1} to t_{R3} are only possible ~~from 28 to 34 s~~for periods between 28 and 34s. This method was tested and found to be effective in a pre-mission blind test (Clinton et al., 2017; van Driel et al., 2019). Method 3 is a multiple filter technique implemented in the Computer Programs in Seismology (Herrmann, 2013) to calculate the envelope energy on the vertical component of the seismogram, and the preferred arrival time corresponds to the maximum energy at different periods and time windows. For R1, picks are made for periods from 16.3 to 40.9 s, but picks for R1-R3 are only available for periods from 25.3 to 34.6 s. Method 4 derived arrival times at periods between 39 and 19s by applying the multiple filter technique (Dziewonski et al., 1969) in the implementation of Meier et al. (2004) to the vertical-component seismogram and, for each period, picking the amplitude maxima in time windows around the R1, R2 and R3 phases.

While R1 shows clear dispersion, which can be used to model seismic structure along the minor arc as a function of depth, the picks for both R2 and R3 are visible over a much narrower frequency band, and show little or no dispersion. Because of this lack of dispersion and the presence of other potential signals of similar amplitude near the preferred R2 observation, we also consider a second window for R2. ~~An alternate possible set of picks for R2 of a similar amplitude to the R2 we used, arriving~~The alternate R2 arrives roughly 300 seconds later (Fig. 1G), and shows potential evidence of dispersion. However, this interpretation is not favored. The envelopes in this time window are complicated with multiple peaks, ~~and an R2 arriving that much later would suggest~~and this pick suggests a location significantly closer (roughly 8 degrees) than that determined by MQS using the body wave timing (Kawamura et al., 2022). Additionally, the waveforms in different frequency bands do not show consistent elliptical polarization with no clear relationship to the backazimuth estimated from the MQS body wave polarization (Fig. 2D). For this reason, we use the R2 arrival times as shown in Fig. 1E.

Using the travel times estimated in narrow frequency band windows, we can use all frequency bands for which we can pick ~~R1-R3~~t_{R1}-t_{R3} to estimate the epicentral distance and origin time using equations 1-3. These results as well as the estimated great-circle average Rayleigh wave group velocity are shown for all four methods of picking group arrivals in Fig. 3. For each method, the standard deviation across the different frequency band estimates is shown ~~as 1σ error bounds~~. The summary value is defined by the average across the different picking methods and the standard deviation of those methods. For epicentral distance and origin time, these are compared with the MQS estimates from body wave observations shown with shading to indicate the ~~2σ~~ uncertainty ~~bounds derived from the best-fitting Gaussian to the non-Gaussian probability density function estimated with the MQS approach~~defined by the MQS method, described in more detail in Kawamura et al. (2022).

3 Rayleigh wave ellipticity and backazimuth estimation

In Panning et al. (2015), backazimuth estimation using Rayleigh wave energy on Earth events was performed using both a broadband window over all measured frequency bands, as well as averaging the narrow band backazimuth estimations with similar accuracy, although the broadband estimation showed slightly smaller mismatch across the events studied. For each prospective backazimuth in Fig. 2, we rotate a horizontal component such that motion along that backazimuth pointing towards the prospective source is positive. Correlation is calculated with the Hilbert transform of the vertical component, and should reach a maximum at the correct backazimuth. Note that this convention for the horizontal component is the opposite of the radial component of the standard seismological ZRT coordinate system which is defined positive in the direction from source to receiver, which would be negatively correlated with the Hilbert-transformed vertical component for standard retrograde elliptical Rayleigh wave particle motion. The narrowness of the correlation peak, however, was strongly dependent on the presence or
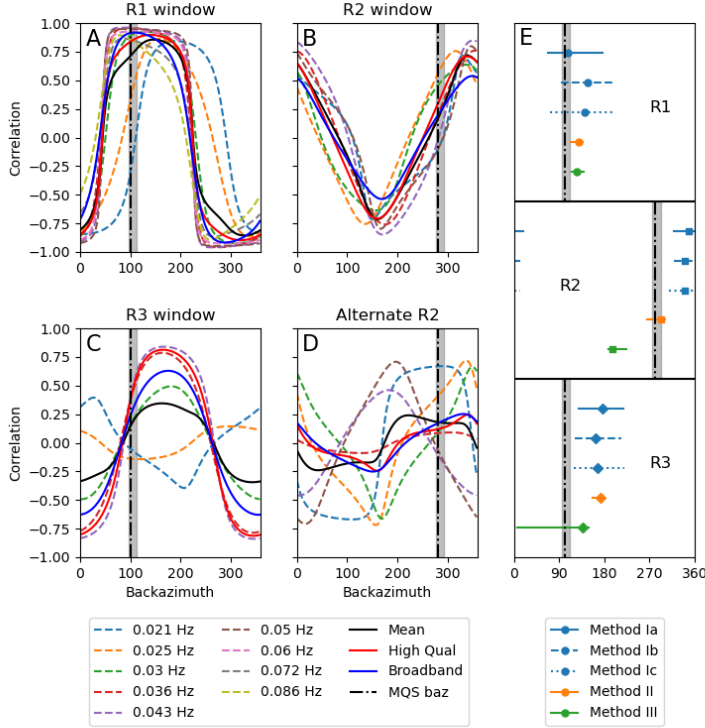
Figure 2. Backazimuth estimation for each Rayleigh wave arrival. For each backazimuth, correlation is calculated between the horizontal component positive in the direction of the proposed backazimuth and the Hilbert transform of the vertical component. Correlations are calculated on narrow band waveforms in time windows centered on the pick times shown in Fig. 1 with a width of 4 dominant periods. For the broadband waveforms, correlations are calculated over 200 second windows beginning at 450 seconds after the P arrival time for R1 (A), 6250 seconds for R2 (B), 7825 seconds for R2 (C), and 6550 seconds for the alternate R2 time (D). (E) Summary of backazimuth determined from R1, R2, and R3. Methods Ia-Ic are based on the results shown in panels (A)-(D) for the broadband, mean over the frequency bands, and average over the high quality measurements, respectively. Methods II and III are independent approaches described in the text. In all panels, the MQS backazimuth is shown with the dot-dash line with uncertainty shaded in gray.

absence of Love wave energy in the measurement window (Panning et al., 2015). While Love wave energy is seen for this event (Kawamura et al., 2022; Kim, Ceylan, et al., 2022; Li et al., 2022; Beghein et al., 2022), it arrives in a non-overlapping time window with the Rayleigh energy ~~analyzed here~~, and so estimated correlation peaks are generally ~~quite~~ broad (Fig. 2). In Fig. 2E, we show three backazimuths from this correlation-based method (Methods Ia-Ic), which correspond to the correlation computed over broadband data, the average over all narrow-band data, and only over 'high-quality' data. Note that we number the different approaches to back-azimuth estimation with Roman numerals to differentiate from the different surface wave arrival estimations numbered with Arabic numerals. High-quality data excludes measurement windows which do not have clear peaks or have multiple peaks of similar amplitude in the enveloped data (see table in supplementary material for specific frequencies identified as lower quality). In each case, the range of possible backazimuths shown in ~~the figure~~ Fig. 2 represent the range with correlation above 80% of the maximum value. We also show estimates for two additional methods. Method II is based on the maximization of the ground-motion amplitudes on the Z and R components around the arrival time of the Rayleigh waves for different frequencies. The preferred back-azimuths are derived from the maximum of the Z*R/T coefficient, which is computed from seismogram envelopes. This method has a 180 deg uncertainty, which is resolved by assessing the phase shift between the Z and R components, obtained from their maximum cross-correlation. The ~~definitive~~ back-azimuth of each Rayleigh wave is the median obtained from the frequencies for which Rayleigh energy is observed and for which mainly retrograde motion is determined (phase shift > 0). See Carrasco et al. (2022) for details. Method III uses several independent approaches to obtain frequency-dependent polarization and backazimuth estimates of surface wave arrivals. This method has been previously implemented to extract seismic signals that are strongly elliptically polarized and traveling along the great circle path, leading to the first detection of Rayleigh waves on Mars (Kim, Banerdt, et al., 2022). See Kim, Ceylan, et al. (2022) for details.

The broadband estimation of the correlation for R1 (Method Ia), as well as Methods II and III peak ~~very~~ close to the MQS backazimuth determined using body waves (solid blue line in Fig. 2A), but the averages over the narrowband estimates (Methods Ib and Ic) have a ~~very~~ broad peak that reach a maximum value 30-40 degrees to the south of the MQS estimate. With the much lower signal to noise ratio (SNR) for R2, the backazimuths are more variable between methods with Methods Ia-Ic shifted significantly to the north, while Method III is shifted to the west, but the methods do bracket the predicted azimuth from the MQS body wave event azimuth. On the other hand, the potential alternate R2 time, which shows ~~a little more dispersion~~more apparent dispersion than the preferred R2 arrival, does not show strong correlation peaks indicating elliptical particle motion, and the weak peaks that are observed show no consistency between different frequency bands. This strongly supports that this window does not contain the major R2 energy, and thus should not be used for location or structure estimation. Finally, the R3 backazimuth estimates are shifted to the south for all five methods considered, but ~~signal-to-noise ratio~~SNR is fairly low for this observation, and the fact that elliptical motion does seem to be resolved in all methods at least gives credence to interpreting this arrival as R3. It is, however, important to note that ~~this event~~S1222a occurs during the noisy season on Mars, and therefore the ~~signal to noise ratio~~SNR for R2 and R3 are low. Both ellipticity and backazimuth estimations are more challenging and can be biased in this situation as wind effects can mimic the elliptical motion of Rayleigh waves or even generate surface waves at different azimuths (e.g. Stutzmann et al., 2021)~~, and this.~~ This may contribute to both the offset of these backazimuth estimates from the MQS backazimuth as well as the scatter between the different methods.
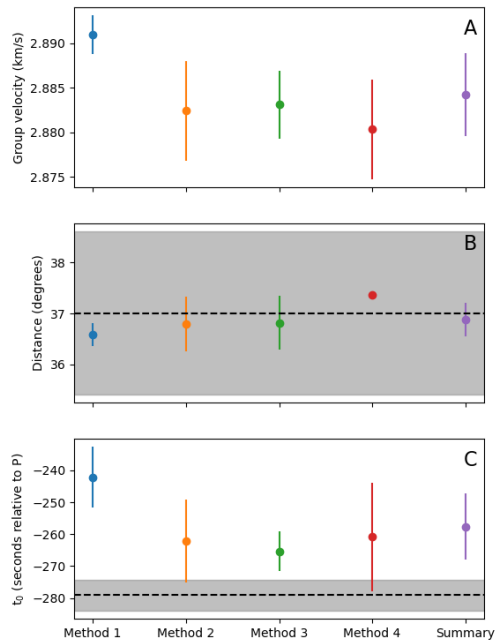
Figure 3. For each of the four methods employed, the average value and standard deviation across the individual narrow band frequencies measured is shown for the group velocity (A), epicentral distance (B), and origin time (C) calculated from equations 1-3. Dashed black lines represent the MQS estimated epicentral distance and origin time (Kawamura et al., 2022), while the grey shaded box represents ~~the 2σ~~ error bounds ~~estimated based on the best-fitting Gaussian to the non-Gaussian uncertainties estimated by the MQS location procedure~~<u>from</u> Kawamura et al. (2022).

4 Results

The epicentral distance determined for all the sets of surface wave arrival times is 36.9° with a standard deviation of 0.3°. Note that this standard deviation represents only the variation of distance estimates based on different surface wave measurement approaches, and likely underestimates the total uncertainty in distance which should also include additional uncertainty due to 3D variation in seismic velocity, or possible biases in the measured surface wave arrival times due to effects such as interference with removed glitches. ~~are~~This estimate is in good agreement with the body-wave based MQS value. All surface wave estimates ~~but one~~ are within the ~~2 sigma~~ uncertainty bounds obtained by the MQS $(37° ± 1.6°)$ (Kawamura et al., 2022), while the MQS estimate agrees within one standard deviation with the mean surface wave epicentral distance calculated across different methods.

The backazimuth estimated from the R1 broadband measurement of 108° is consistent with the MQS backazimuth uncertainty bounds $(96° − 112°)$ ~~When taking into account the full location obtained using the surface wave-based distance estimate and the backazimuth determined from the R1 broadband measurement, the surface wave epicentral location agrees with the MQS estimate within a degree which is well within the 2 sigma uncertainty bounds.~~ However, if the average over the high quality narrow band estimates is used instead (which provided similar accuracy for the Earth data analyzed in Panning et al. (2015)), the 32 degree mismatch in backazimuth calculation (108 for the broadband vs. 140 for the average over high quality narrow band estimates) ~~leads to an absolute location mismatch of 18.5 degrees outside the 2 sigma uncertainty bounds of the MQS estimate, which is unsurprising as 140 degrees is outside the 2 sigma error bounds of the MQS backazimuth value (109 +/ 14.9 degrees)~~is outside the uncertainty bounds estimated by the MQS. When combining the distance and backazimuth estimates, the location using the broadband backazimuth estimate is offset from the nominal MQS location by ∼4° (Fig. 4, magenta diamond), while backazimuth based on the average across measurements leads to location that differs from the nominal MQS location by ∼23° (Fig. 4, cyan diamond) which is well outside the estimated uncertainty of the MQS location (blue dot and ellipse in Fig. 4).

The origin time determination for all surface wave methods is roughly 20 seconds later than the MQS origin time estimate. Some possible explanations for the mismatch between estimated origin time are considered in the Discussion section. An offset of origin time of 20 seconds is also quite consistent with the range of offsets observed for Earth events located with this method by Panning et al. (2015) which were generally offset from catalog origin times within ±30s. Additionally, that study showed that origin time offsets compared with catalog origin time often significantly exceeded the standard deviation of origin time estimates across different frequency bands, so the lack of overlap of the standard deviations in Fig. 3C with the MQS t_0 should not be surprising.

5 Discussion

The results show ~~very~~ close agreement in distance estimation between the MQS body wave determination and that derived from the multi-orbit surface waves, which do not depend ~~at all~~ on a priori velocity models, beyond the assumption of spherical symmetry. This provides important validation of the MQS method that has been utilized for many events now and performed ~~quite~~ well. The MQS body wave method's success includes accurately providing location estimates for impacts within 300 km of the lander in order to target HiRISE images showing new craters (Garcia et al., 2022) as well as larger, more distant impacts with craters detected by the CTX camera aboard MRO (Posiolova et al., 2022). However, the difficulty in matching backazimuth between P- and surface waves shows that the latter may be affected by off-great-circle propagation due to three-dimensional (3D) structure, particularly as this path does cross the dichotomy
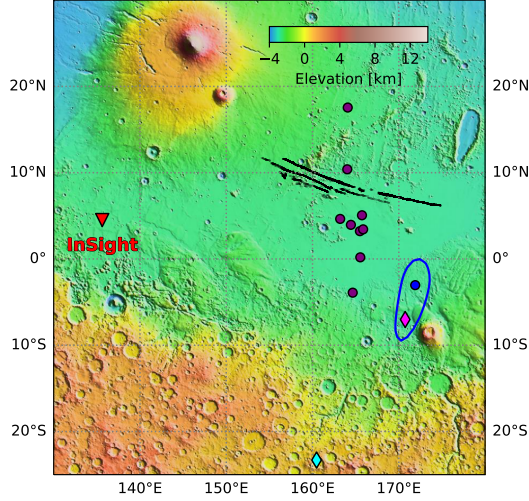
Figure 4. Estimated locations of S1222a from MQS (Kawamura et al., 2022, blue circle with uncertainty shown with blue ellipse), based on the multi-orbit distance estimation and the back-azimuth estimated from the broadband polarization of R1 (magenta diamond), and based on the backazimuth estimated from the average of the correlation functions across the high-quality narrow band frequency estimates (cyan diamond). Purple dots show other events located by MQS. Figure is adapted from Kawamura et al. (2022).

between the northern and southern hemispheres of Mars at a relatively shallow angle. R2 and R3 backazimuths also show apparent offsets from the MQS backazimuth, but these are in general much more poorly resolved due to lower SNR (e.g. Kim, Ceylan, et al., 2022). The t_0 mismatch may also be related to 3D structure. For example if the R1 path were a little slower than the great-circle average group velocity, one might expect that the R1 would arrive a little late, and thus a t_0 estimated from equation 3, would be correspondingly late. ~~Given that R1 only runs over 10% of the circumference of the planet, it is plausible that its group velocity is least representative of the global average.~~ If we look at measured arrival times near 0.03Hz, and we assume the MQS location and origin time is correct and all surface wave propagation is along the great circle path, the velocity of R2 is ~0.7% faster than R1. However, the great-circle average velocity calculated as the path-length weighted average of the R1 and R2 velocities is ~0.4% slower than the great-circle averaged velocity computed from the difference between t_{R3} and t_{R1}, suggesting that we cannot simply explain the difference between estimated origin times through assuming the MQS origin time is correct and all differences in the surface wave estimation is due to different minor arc and major arc velocity. Likely the true explanation relates to some combination of differences in minor and major arc velocity, offsets in true distance and origin time within the uncertainties of the MQS estimates, and possible small biases in the estimates of t_{R3}-t_{R1}, as may happen due to interference from glitches or other causes. ~~However, in order to match the great-circle average velocity, the R2 path would need to be faster, and therefore we would expect R2 to arrive a little earlier than predicted from the MQS location. It actually also arrives later than predicted from the MQS origin time and the great-circle average velocity, though, although perhaps the off-great-circle propagation possibly suggested by the azimuth estimations along both arcs could contribute to the late arrivals. This means that shifting the picks of R2, where there are some arrivals of similar amplitude before or after the picks we went with in this study cannot resolve the offset between MQS origin time, and that estimated from surface waves.~~

6 Conclusion

Consistent with pre-mission expectations on observability of surface waves circling Mars, the $M_W 4.7$ S1222a marsquake was large enough to make observations of multiple-orbit Rayleigh waves. These were used to apply a location method that does not depend on *a priori* velocity structure, and the recovered distance and broadband backazimuth estimate agree well with the standard MQS body-wave based approach, providing additional verification of the location approach used for the bulk of events observed in the InSight mission.

Open Research

All raw waveform data is available through the InSight Mars SEIS Data Service @ IPGP, IRIS-DMC and NASA PDS. (InSight Mars SEIS Data Service, 2019). All processed data and processing codes used in this study are available through `https://github.com/mpanning/R1R2R3_data_codes` (doi to be provided before manuscript is finalized).

References

Bagheri, A., Khan, A., Al-Attar, D., Crawford, O., & Giardini, D. (2019). Tidal response of Mars constrained from laboratory-based viscoelastic dissipation models and geophysical data. *J. Geophys. Res. Planets*.

Banerdt, W. B., Smrekar, S., Banfield, D., Giardini, D., Golombek, M., Johnson, C., ... Wieczorek, M. (2020). Initial results from the InSight mission on Mars. *Nature Geoscience*, *13*, 183–189. doi: 10.1038/s41561-020-0544-y

Beghein, C., Li, J., Weidner, E., Maguire, R., Wookey, J., Lekic, V., ... Banerdt, W. B. (2022). Crustal anisotropy in the martian lowlands from surface wave. *Geophys. Res. Lett.*, *49*, e2022GL101508. doi: 10.1029/2022GL101508

Brinkman, N., S. Stähler, S. C., Giardini, D., Schmelzbach, C., Khan, A., Jacob, A., ... Banerdt, W. B. (2021). First focal mechanisms of marsquakes. *Journal of Geophysical Research: Planets*, *126*(4), e2020JE006546. doi: 10.1029/2020JE006546

Carrasco, S., Knapmeyer-Endrun, B., Margerin, L., Xu, Z., & Charalambous, C. (2022). *Crustal martian structure from the analysis and inversion of large-marsquakes Rayleigh waves ellipticity.* Abstract presented at American Geophysical Union, Fall Meeting 2022.

Ceylan, S., Clinton, J. F., Giardini, D., Böse, M., Charalambous, C., van Driel, M., ... Perrin, C. (2021). Companion guide to the marsquake catalog from InSight, sols 0–478: Data content and non-seismic events. *Phys. Earth Planet. Int.*, *310*,

106597. doi: 10.1016/j.pepi.2020.106597

Ceylan, S., Clinton, J. F., Giardini, D., Stähler, S. C., Horleston, A., Kawamura, T., . . . Banerdt, W. B. (2022). The marsquake catalogue from insight, sols 0–1011. *Physics of the Earth and Planetary Interiors*, 106943. doi: 10.1016/j.pepi.2022.106943

Clinton, J. F., Ceylan, S., van Driel, M., Giardini, D., Stähler, S. C., Böse, M., . . . Stott, A. E. (2020). The Marsquake catalog from InSight, sols 0–478. *Phys. Earth Planet. Int.*, *310*, 106595. doi: 10.1016/j.pepi.2020.106595

Clinton, J. F., Giardini, D., Böse, M., Ceylan, S., van Driel, M., Euchner, F., . . . Teanby, N. A. (2018). The Marsquake Service: Securing daily analysis of SEIS data and building the martian seismicity catalogue for InSight. *Space Sci. Rev.*, *214*, 133. doi: 10.1007/s11214-018-0567-5

Clinton, J. F., Giardini, D., Lognonné, P., Banerdt, W. B., van Driel, M., Drilleau, M., . . . Spiga, A. (2017). Preparing for InSight: An invitation to participate in a blind test for Martian seismicity. *Seis. Res. Lett.*, *88*(5), 1290–1302. doi: 10.1785/0220170094

Durán, C., Khan, A., Ceylan, S., Charalambous, C., Kim, D., Drilleau, M., . . . Giardini, D. (2022). Observation of a core-diffracted P-wave from a farside impact with implications for the lower-mantle structure of Mars. *Geophysical Research Letters*, *49*(21), e2022GL100887. doi: 10.1029/2022GL100887

Dziewonski, A., Bloch, S., & Landisman, M. (1969). A technique for the analysis of transient seismic signals. *Bull. seism. Soc. Am*, *59*, 427–444.

Garcia, R. F., Daubar, I. J., Beucler, E., Posiolova, L., Lognonné, P., Rolland, L., . . . Banerdt, W. B. (2022). Newly formed craters on Mars located using seismic and acoustic wave data from InSight. *Nature Geoscience*. doi: 10.1038/s41561-022-01014-0

Giardini, D., Lognonné, P., Banerdt, W. B., Christensen, U., Clinton, J., van Driel, M., . . . Yana, C. (2020). The seismicity of Mars. *Nature Geoscience*, *13*, 205–212. doi: 10.1038/s41561-020-0539-8

Herrmann, R. B. (2013). Computer programs in seismology: An evolving tool for instruction and research. *Seis. Res. Lett.*, *84*, 1081–1088. doi: 10.1785/0220110096

Horleston, A. C., Clinton, J. F., Ceylan, S., Giardini, D., Charalambous, C., Irving, J. C. E., . . . Banerdt, W. B. (2022). The far side of Mars: Two distant marsquakes detected by InSight. *The Seismic Record*, *2*(2), 88–99. doi: 10.1785/0320220007

InSight Mars SEIS Data Service. (2019). *Seis raw data, InSight mission.* IPGP, JPL, CNES, ETHZ, ICL, MPS, ISAE-Supaero, LPG, MFSC. doi: 10.18715/seis.insight .xb_2016

InSight Marsquake Service. (2022). *Mars seismic catalogue, InSight mission; v12 2022-10-01 (version 12.0).* ETHZ, IPGP, JPL, ICL, Univ. Bristol.

Jacob, A., Plasman, M., Perrin, C., Fuji, N., Lognonné, P., Xu, Z., . . . Banerdt, W. B. (2022). Seismic sources of InSight marsquakes and seismotectonic context of Elysium Planitia, mars. *Tectonophysics*, *837*, 229434. doi: 10.1016/j.tecto.2022.229434

Kawamura, T., Clinton, J. F., Zenhäusern, G., Ceylan, S., Horleston, A. C., Dahmen, N. L., . . . Banerdt, W. B. (2022). Largest marsquake ever detected by InSight: S1222a. *Geophys. Res. Lett.*, *49*, e2022GL101543. doi: 10.1029/2022GL101543

Khan, A., Liebske, C., Rozel, A., Rivoldini, A., Nimmo, F., Connolly, J. A. D., . . . Giardini, D. (2018). A geophysical perspective on the bulk composition of mars. *Journal of Geophysical Research: Planets*, *123*(2), 575-611. doi: 10.1002/2017JE005371

Khan, A., van Driel, M., Böse, M., Giardini, D., Ceylan, S., Yan, J., . . . Banerdt, W. B. (2016). Single-station and single-event marsquake location and inversion

for structure using synthetic Martian waveforms. *Phys. Earth Planet. Int.*, *258*, 28–42. doi: 10.1016/j.pepi.2016.05.017

Kim, D., Banerdt, W. B., Ceylan, S., Giardini, D., Lekić, V., Lognonné, P., . . . Panning, M. P. (2022). Surface waves and crustal structure on Mars. *Science*. (accepted)

Kim, D., Ceylan, S., Stähler, S. C., Lekic, V., Maguire, R., Zenhäusern, G., . . . Banerdt, W. B. (2022). Structure along the martian dichotomy constrained by surface waves. *Geophys. Res. Lett.*. (in preparation)

Kim, D., Davis, P., Lekić, V., Maguire, R., Compaire, N., Schimmel, M., . . . Banerdt, W. B. (2021). Potential pitfalls in the analysis and structural interpretation of seismic data from the Mars InSight mission. *Bull. Seism. Soc. Am.*, *111*(6), 2982–3002. doi: 10.1785/0120210123

Krischer, L., Megies, T., Barsch, R., Beyreuther, M., Lecocq, T., Caudron, C., & Wasserman, J. (2015). ObsPy: a bridge for seismology into the scientific Python ecosystem. *Comp. Sci. Disc.*, *8*(1), 014003. doi: 10.1088/1749-4699/8/1/014003

Li, J., Beghein, C., Panning, M. P., Davis, P., Lognonné, P., & Banerdt, W. B. (2022). Different martian crustal seismic velocities across the dichotomy boundary from multi-orbiting surface waves. *Geophys. Res. Lett.*, *49*, e2022GL101243. doi: 10.1029/2022GL101243

Lognonné, P., Banerdt, W. B., Giardini, D., Pike, W. T., Christensen, U., Laudet, P., . . . Wookey, J. (2019). SEIS: The Seismic Experiment for Internal Structure of InSight. *Space Sci. Rev.*, *215*. doi: 10.1007/s11214-018-0574-6

Lognonné, P., Banerdt, W. B., Pike, W. T., Giardini, D., Christensen, U., Garcia, R. F., . . . Zweifel, P. (2020). Constraints on the shallow elastic and anelastic structure of Mars from InSight seismic data. *Nature Geoscience*, *13*, 213–220. doi: 10.1038/s41561-020-0536-y

Meier, T., Dietrich, K., Stöckhert, B., & Harjes, H.-P. (2004). One-dimensional models of shear wave velocity for the eastern mediterranean obtained from the inversion of rayleigh wave phase velocities and tectonic implications. *Geophysical Journal International*, *156*(1), 45–58.

Panning, M. P., Beucler, E., Drilleau, M., Mocquet, A., Lognonné, P., & Banerdt, W. B. (2015). Verifying single-station seismic approaches using Earth-based data: Preparation for data return from the InSight mission to Mars. *Icarus*, *248*, 230–242. doi: 10.1016/j.icarus.2014.10.035

Posiolova, L. V., Lognonné, P., Banerdt, W. B., Clinton, J. F., Collins, G. S., Kawamura, T., . . . Zenhäusern, G. (2022). Largest recent impact craters on Mars: Orbital imaging and surface seismic co-investigation. *Science*. (accepted)

Scholz, J.-R., Widmer-Schnidrig, R., Davis, P., Lognonné, P., Pinot, B., Garcia, R. F., . . . Banerdt, W. B. (2020). Detection, analysis, and removal of glitches from InSight's seismic data from Mars. *Earth Space Sci.*, *7*, e2020EA001317. doi: 10.1029/2020EA001317

Smrekar, S. E., Lognonné, P., Spohn, T., Banerdt, W. B., Breuer, D., Christensen, U., . . . Wieczorek, M. (2019). Pre-mission InSights on the interior of Mars. *Space Sci. Rev.*, *215*, 3. doi: 10.1007/s11214-018-0563-9

Stutzmann, E., Schimmel, M., Lognonné, P., Horleston, A., Ceylan, S., van Driel, M., . . . Spiga, A. (2021). The polarization of ambient noise on Mars. *Journal of Geophysical Research: Planets*, *126*(1), e2020JE006545. doi: 10.1029/2020JE006545

van Driel, M., Ceylan, S., Clinton, J. F., Giardini, D., Alemany, H., Allam, A., . . . Zheng, Y. (2019, 06). Preparing for InSight: Evaluation of the Blind Test for Martian Seismicity. *Seismological Research Letters*, *90*(4), 1518–1534. doi: 10.1785/0220180379